Biol. Cybern. 80, 417–431 (1999)

Biological Cybernetics

Directional coding of three-dimensional movements by the vestibular semicircular canals

Richard D. Rabbitt

Department of Bioengineering, 50S Central Campus Dr. Rm. 2480, University of Utah Salt Lake City, Ut 84112, USA

Received: 26 January 1998 / Accepted in revised form: 26 January 1999

Abstract. A morphologically descriptive mathematical model was developed to study the role of labyrinthine geometry in determining sensitivities of each semicircular canal to angular motion stimuli in three-dimensional (3D) space. For this, equations describing viscous flow of the endolymph and poro-elastic response of the cupulae were coupled together and solved within a 3D reconstructed geometry. Results predict the existence of prime rotational directions about which the labyrinth resolves 3D angular movements into separate vectorial components. The components are predicted to be transmitted to the brain separately, one coded by each canal nerve. Prime directions predicted by the model are non-orthogonal, distinct from the anatomical canal planes, and distinct from the directions of rotation which elicit maximal responses of individual canal nerves. They occur for each canal along the intersection of the two null planes defined by its sister canals. Hence, rotation about a prime direction excites only one canal nerve. This contrasts the situation for rotations about anatomical canal planes, or about maximal response directions, where the model predicts activation of multiple canal nerves. The prime directions are sensitive to labyrinthine morphology and, hence, are predicted to vary between species and, to a lesser extent, vary between individual animals. Prime directions were estimated in the present work using a mathematical model, but could be determined experimentally based on the directional sensitivities of individual canal nerves. The model also predicts the existence of dominant eigenmodes and time constants associated with rotation in each of the prime directions. Results may have implications regarding the central representation of angular head movements in space as well as the neuronal mappings between three-canal afferent inputs and motor outputs.

Correspondence to: R.D. Rabbitt (e-mail: r.rabbitt@m.cc.utah.edu, Tel.: +1-801-5816968 (Lab.:-4549),
internet: http://www.bioen.utah.edu/faculty/RDR)

1 Introduction

The primary function of the vestibular semicircular canals is to encode the direction and temporal pattern of angular head movements and relay the information to the brain. To achieve this goal, the system must construct a representation of a three-dimensional (3D) axial vector which changes length and direction with time. For rotation about a fixed direction, temporal information is encoded by frequency and amplitude dependent responses of individual afferent nerves (Lowenstein and Sand 1940; Goldberg and Fernandez 1971; Fenández and Goldberg 1971; Blanks et al. 1975; Estes et al. 1975; Schneider and Anderson 1976; O'Leary and III 1979; Landolt and Correia 1980; Segal and Outerbridge 1982; Boyle and Highstein 1990; Brichta and Goldberg 1996). Afferent responses of a single canal nerve, however, do not carry sufficient information to determine the direction or absolute magnitude of angular head motion. For this, it is necessary to consider responses from nerves of three or more sensory end organs. We focus here on the semicircular canal ampullary organs. In species ranging from elasmobranchs to primates, labyrinths generally consist of three slender toroidal ducts arranged in roughly orthogonal planes (Gray 1907; Gray 1908; Wersäll and Bagger-Sjöbäck 1974; Graf 1988). As first suggested by Mach (Mach 1875), this specialized morphology is responsible for decomposition of the 3D rotational head movements into three individual components, one associated with each semicircular canal nerve. Recordings from single afferent nerves show the existence of maximal response directions, and corresponding null planes, that are distinct for each canal (Blanks et al. 1975, 1985; Estes et al. 1975; Reinsine et al. 1988; Dickman, 1996). The maximal response direction and so-called sensitivity vectors of canal afferents are well described using a simple 3D cosine rule. The cosine rule follows directly from simple mathematical models of semicircular canal macromechanics dating back to Steinhausen (1933). More recently, Oman et al. (1987) demonstrated that null planes also exist for more complex model geome-

tries. Hence, the evidence continues to support Mach's 1875 proposition: the vestibular labyrinth is sculpted in 3D space to mechanically decompose arbitrary angular head movements into components, one component carried by each canal nerve. This decomposition underlies the ability to sense the magnitude and direction of angular head movement.

Afferent signals from individual ampullary organs are ultimately combined centrally with numerous other sensory inputs for the central representation of head and body movements in 3D space. In the vestibulo-ocular reflex (VOR) and vestibulo-collic reflex (VCR) systems, the central representation must be transformed to match the kinematics and kinetics of motor outputs (Robinson 1982; Ezure and Graf 1984a; Pellionisz and Graf 1987). The specific neuronal architecture and synaptic contacts necessary to implement the proper reflex action depends strongly on how 3D motion is sensed and conveyed centrally. There is evidence suggesting that, at least on a subcortical level, the central nervous system may be organized to represent angular movements primarily using canal-based coordinates. Some regions of the vestibular nuclei receive terminating afferent fibers primarily from individual canals (Lorente de Nó 1933). Anatomical and physiological characteristics of second-order vestibular neurons reveal a strong correspondence to individual canal nerves (Uchino et al. 1979, 1980; McCrea et al. 1980, 1987a,b; Graf et al. 1983, Harai and Uchino 1984, Graf and Ezure 1986; Fukushima et al. 1990). Electrical stimulation of individual canal nerves further indicates that most second-order neurons in the vestibular nuclei receive inputs primarily from one semicircular canal (Suzuki et al. 1969; Curthoys and Markham 1971; Markham and Curthoys 1972; Sans et al. 1972; Wilson and Felpel 1972; Kashara and Uchino 1974; Abend 1977). These same neurons also receive critical inputs from the visual system (Waespe and Henn 1977; Fukushima et al. 1990), thus indicating that 3D multisensory convergence takes place partially in the canal-based directions (Collewijn 1975; Hoffmann 1982; Hoffmann 1988). The canal-based directions also appear to be utilized by the visual system, at least on the sub-cortical level (Graf 1988; Simpson et al. 1988). This has important general implications regarding ocular, postural and motor control (Berthoz and Grantyn 1986; Vidal et al. 1986; Cohen 1988; Peterson et al. 1992). There is evidence that the canal-based representation also extends to the cerebellum (Ito 1984, Graf 1988). It is, therefore, critical to precisely understand what the canal-based coordinate system is and how it is predetermined by the morphology and macromechanics of the labyrinth.

Mach (1875) focused attention on the physiological role of anatomical canal planes. The introduction of single-unit recording techniques has since shown that canal planes are not precisely aligned with maximal response directions of individual afferents. Directions of maximal sensitivity are reported to differ from anatomical canal planes by an average of $\approx 7^\circ$ in cat (Estes et al. 1975) and $\approx 6^\circ$ in monkey (Reisine et al. 1988). In pigeon, the average difference is reported to be $\approx 10^\circ$ in the horizontal canal (HC), $\approx 8^\circ$ in the posterior canal (PC) and $\approx 26^\circ$–56° in the anterior canal (AC) (Dickman 1996). Discrepancies are even larger when individual animals are considered rather than averages (Reisine et al. 1988). Clearly canal planes do not represent the coordinate system used to decompose 3D angular head movements. Therefore, models often use the maximal response directions of the nerves to decompose angular head movements into three components. Maximal response directions, however, do not fall precisely in the null planes of the sister canals (Estes et al. 1975; Reisine et al. 1988; Dickman 1996). The fact that rotation about a single maximal response direction excites the sister canals shows that these directions are not actually used by the labyrinth to parse the 3D motion into components associated with each nerve. The afferent nerves must be representing the direction of rotation in some other way.

In the present work we seek to describe natural coordinates of the three-canal vestibular labyrinth that constrain the way in which directional information is sensed and represented. For this purpose, a new mathematical model was developed to describe endolymph flow and cupular dynamics in the morphologically correct 3D membranous labyrinth. The model was then applied to determine prime directions which are predicted to be the directions used by the canals to decompose angular movements into components represented in each canal nerve. An asymptotic solution of the Navier-Stokes equations previously derived by Damiano and Rabbitt (1996) was used to model endolymph fluid dynamics within each continuous duct of the membranous labyrinth. This approach provides results similar to that of Oman et al. (1997) and has been applied previously to single canals (Damiano and Rabbitt 1996; Oman et al. 1987). In the present work, flow in the HC, AC, PC, common crus (CC) and utricular segments were coupled together at the bifurcation points using conservation of fluid mass and continuity of pressure. Equations describing the fluid were further coupled to poro-elastic models for the cupulae thus providing a closed system of equations.

2 Model geometry

The model requires, as an input, the full 3D geometry of the membranous vestibular labyrinth. The only complete 3D reconstruction appearing in the literature to date is for a teleost fish, the oyster toadfish *Opsanus tau* (Ghanem et al. 1998). We therefore applied the model to this species to generate specific results for discussion. The gross morphology of the system is remarkably preserved across species to such an extent that the toadfish labyrinth is quite similar to that of primates and human (Igarashi 1967; Igarashi et al. 1981, Igarashi et al. 1983; Ghanem et al. 1998). Prime directions and model predictions will, of course, vary for other species, but the concepts should be universal across a very broad spectrum of animals. Figure 1 shows the geometry of the right toadfish membranous labyrinth. Figure 1A provide two views of a surface reconstruction of the right labyrinth indicating the HC, AC and PC. Figure1-

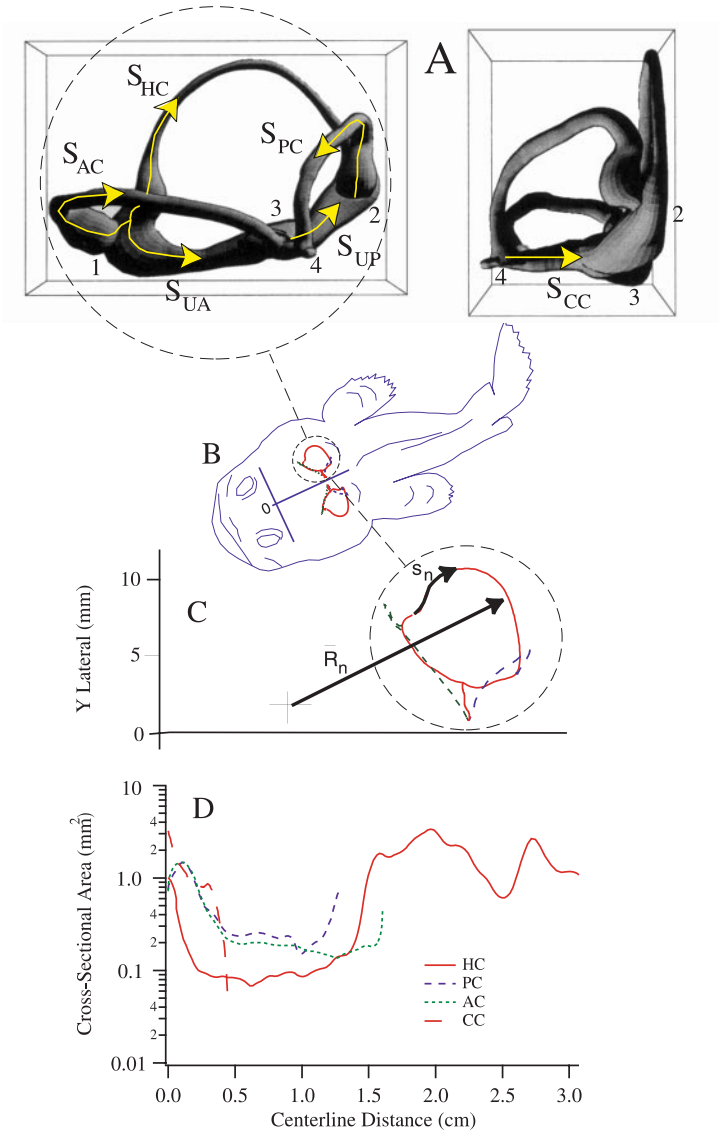

Fig. 1A–D. Model geometry. The membranous labyrinthine model geometry is illustrated as dorsal and caudal views (**A**). Centerlines of the horizontal canal (*HC*, *solid*), anterior canal (*AC*, *short-dashed*) and posterior canal (*PC*, *long-dashed*) are shown relative to the fish in **B** and expanded in **C**. $\vec{R}_n$ is a vector running from the axis of rotation to the centerline of each canal segment. The trajectories of $\vec{R}_n$ define the centerline coordinates s_n. Centerlines for the HC, AC and PC originate at the cupulae and run in the direction of the duct lumen, while the centerline of the common crus (*CC*) has its origin at the utricular vestibule and runs in the direction of the crus apex. Cross-sectional area functions for the HC, AC, PC and CC of the right labyrinth are shown in **D** as a functions of the centerline coordinates

B,C are dorsal views illustrating the orientation of the labyrinth in the head relative to the lateral line "T" ridge with "0" denoting the origin of the skull fixed coordinate system. The solid curve indicates the centerline of the HC, the short dashed curve indicates the centerline of the AC and the long dashed curve indicates the curved centerline of the PC. Curved s_n coordinates are defined to run along each of these centerlines with origins at the respective cupulae. Local cross-sectional dimensions of each of the canals and the CC were taken from the reconstruction to determine the cross-sectional area functions provided in Fig. 1D. These cross-sectional area functions and centerline coordinates are used directly in the present model. In the present numerical results, rotation of the head was about the midline directly between the left and right labyrinths.

3 Model for the endolymph

We assume that the membranous labyrinth is perfectly rigid and attached securely to the skull. Head movements are therefore transmitted directly, without modification, to the membranous ducts. We further assume that the ducts are filled with an incompressible viscous fluid undergoing unsteady Stokes flow. Each segment of labyrinth is modeled as a curved tube undergoing prescribed angular and linear accelerations. The acceleration gives rise to inertial forces which are counteracted by pressure and viscous shear stresses. In the present model, we are interested only in the macromechanical fluid displacements within each duct and ampullae, and hence it is sufficient to integrate the velocity distribution across the cross-sectional area and consider only the volume flow rate. Since each duct segment is modeled as perfectly rigid, the volume flow is constant along the segment but the fluid velocity changes in magnitude to account for changes in cross-sectional area. These features have been previously modeled by Oman et al. (1987) and Damiano and Rabbitt (1997) to arrive at a relatively simple second-order differential equation relating the endolymph volume displacement Q_n to head movements and pressure gradients. The model for each uninterrupted segment of the duct takes the form

$$m_n \frac{\mathrm{d}^2 Q_n}{\mathrm{d}t^2} + c_n \frac{\mathrm{d}Q_n}{\mathrm{d}t} + k_n Q_n = P_n(l_n) - P_n(0) + f_n \ , \qquad (3.1)$$

where the parameters m_n, c_n and k_n are the equivalent mass, damping and stiffness of the nth segment. Values of these parameters are directly determined from the 3D morphology and physical constants using (Oman et al. 1987; Damiano and Rabbitt 1996)

$$m_n = \left(\int_0^{l_n} \frac{\rho}{A(s)} \mathrm{d}s \right), \qquad (3.2)$$

$$c_n = \left(\int_0^{l_n} \frac{\mu\lambda}{A(s)^2} \mathrm{d}s \right) \ , \qquad (3.3)$$

and

$$k_n = \left(\int_0^{l_n} \frac{\gamma\lambda}{A(s)^2} \mathrm{d}s \right) \ . \qquad (3.4)$$

The curved coordinate $0 \le s_n \le l_n$ runs along the centerline of the duct segment. $A(s)$ is the cross-sectional area as a function of the curved centerline coordinate. ρ is the density, μ is the viscosity and γ is the shear stiffness of the endolymph (Note that $\gamma = 0$ for a linear Newtonian fluid). The factor λ is a non-dimensional number that relates the volume flow rate to shear stress acting on the wall. It appears in both expressions for the equivalent damping and the equivalent stiffness. In the present model, we assume Poiseuille flow such that $\lambda = 8\pi$. This assumption is appropriate for low frequencies of head movement such as volitional movements (Oman et al. 1987; Damiano and Rabbitt 1996). It is notable that the effective mass is proportional to the inverse of the cross-sectional area while the effective damping is proportional to the inverse of the cross-sectional area squared. Hence, slender regions of each duct dominate determination of coefficients. In addition to terms on the left hand side of Eq. (3.1), a pressure gradient $P_n(l_n) - P_n(0)$ and an inertial forcing term f_n appear on the right. The inertial forcing is

$$f_n = \int_0^{l_n} \rho \left[\vec{A} + \left(\ddot{\vec{\Omega}} \times \vec{R}(s) \right) + \dot{\vec{\Omega}} \times \left(\dot{\vec{\Omega}} \times \vec{R}(s) \right) \right] \cdot \mathrm{d}\vec{s} \ , \qquad (3.5)$$

where $\vec{A}(t)$ is the acceleration of the origin of the head-fixed coordinate system relative to a ground-fixed inertial frame. The vector $\vec{\Omega}$ is the angular velocity and $\ddot{\vec{\Omega}}$ is the angular acceleration of the head relative to the inertial frame, both resolved into vectorial components in the head-fixed system. The vector $\vec{R}(s)$ runs from the head-fixed origin to the local duct centerline. Since the length of $\vec{R}$ is constant in time, Coriolis and linear terms associated with the rate of change of length of $\vec{R}(s)$ do not appear in Eq. (3.5) (Coriolis, linear, tangential and centripetal terms terms may appear in $\vec{A}(t)$ depending on the particular coordinate system and stimulus used). The second and third terms in Eq. (3.5) are due to angular acceleration and angular velocity of the head-fixed system relative to the inertial system and are denoted as the tangential and centripetal accelerations of the membranous labyrinth, respectively. Inertial forces associated with movement of the fluid relative to the duct arise on the left hand side of Eq. (3.1) (Damiano and Rabbit 1996). In the present model, $\vec{A}(t)$ and $\vec{\Omega} \times [\vec{\Omega} \times \vec{R}(s)]$ acceleration components contribute to the local pressure in the ducts but actually do not influence the displacement of cupulae. This is because they cause exactly the same pressure changes on both sides of each cupulae. Proof of this reduction for the case of a rigid membranous duct is provided following Eq. (5.22). Hence, in the present model, it is sufficient to use

$$f_n = \int_0^{l_n} \rho \left(\ddot{\vec{\Omega}} \times \vec{R}(s) \right) \cdot \mathrm{d}\vec{s} \ . \qquad (3.6)$$

Note that this simplification would not be valid if membranous duct flexibility had been included. For 3D motions it is important to note the difference between angular positions resolved in the head-fixed system versus the ground-fixed system. The components of angular acceleration vector in the head-fixed system are determined from the inertial acceleration vector by application of the orthonormal rotation matrix $\mathbf{M}$ following

$$\ddot{\vec{\Omega}} = \mathbf{M} \ddot{\vec{\Omega}}_{\text{inertial}} \qquad (3.7)$$

where $\ddot{\vec{\Omega}}_{\text{inertial}}$ is the angular acceleration written in the ground-fixed inertial reference frame and $\ddot{\vec{\Omega}}$ is the same acceleration vector resolved into the head-fixed system. For rotations about fixed axes, the coordinate system can be selected to render $\mathbf{M}$ the identity matrix, so $\mathbf{M}$ is not needed for rotations about fixed axes.

Versions of Eqs. (3.1)–(3.6) have been applied previously to model endolymph fluid mechanics in the horizontal canal (Oman et al. 1987; Damiano and Rabbitt 1996). In these models endolymph flow is assumed to be restricted to a single canal. Coefficients are determined by integrating Eqs. (3.2)–(3.6) around the closed loop formed by the centerline of the canal. Since the centerline s returns to its origin the pressure gradient $\Delta P = P_n(l_n) - P_n(0)$ appearing in Eq. (3.1) is simply the pressure gradient acting across the cupula. This results in a simple second-order differential equation for the volume displacement Q when combining the fluid equations with a simple spring-mass-damper model of the cupula. The system is highly overdamped, corresponding to low Reynolds' number flow, due to the viscosity of the endolymph and small dimensions of the canal duct.

In the present analysis, we apply Eqs. (3.1)–(3.6) to all three canals. In the toadfish, the labyrinth has four natural bifurcations (1–4, Fig. 1A) that define six individual segments. The first segment defines the HC and ampulla, the second defines the AC and ampulla, the third defines the PC and ampulla, the fourth defines the CC, the fifth defines the anterior section of the utricular vestibule (UA) and the sixth defines the pos-

terior section of the utricular vestibule (UP). This defines six curved centerline coordinates s_n, where n denotes the segment (n = HC, AC, PC, CC, UA, UP). We further divide each canal segment at the center of each ampulla in order to solve for the pressure differential acting across the cupulae. Each segment is modeled using the Eqs. (3.1)–(3.6) as a slender duct, curved in space, and subject forces associated with head movements. The pressures, P_n, and endolymph volume displacements, Q_n^{e}, appearing in these equations are related to one another by pressure continuity and conservation of fluid volume at each of the four bifurcation points. The superscript "e" denotes the endolymph. Using continuity of pressure and conservation of volume we can eliminate the pressure gradients and reduce the number of dependent variables to three. After some algebra we find

$$\mathbf{M}^{\mathrm{e}}\frac{\mathrm{d}^2\vec{Q}^{\mathrm{e}}}{\mathrm{d}t^2}+\mathbf{C}^{\mathrm{e}}\frac{\mathrm{d}\vec{Q}^{\mathrm{e}}}{\mathrm{d}t}+\mathbf{K}^{\mathrm{e}}\vec{Q}^{\mathrm{e}}=\vec{F}^{\mathrm{e}}-\Delta\vec{P}\ , \tag{3.8}$$

where the vector $\vec{Q}^{\mathrm{e}}$ contains the volume displacements of the three cupulae

$$\vec{Q}^{\mathrm{e}}=\begin{bmatrix}Q^{\mathrm{e}}_{\mathrm{HC}}\\ Q^{\mathrm{e}}_{\mathrm{AC}}\\ Q^{\mathrm{e}}_{\mathrm{PC}}\end{bmatrix}\ , \tag{3.9}$$

and the vector $\Delta\vec{P}$ contains the three transcupular pressure gradients

$$\Delta\vec{P}=\begin{bmatrix}\Delta P_{\mathrm{HC}}\\ \Delta P_{\mathrm{AC}}\\ \Delta P_{\mathrm{PC}}\end{bmatrix}\ . \tag{3.10}$$

The mass, damping and stiffness matrices are

$$\mathbf{M}^{\mathrm{e}}=\begin{bmatrix}m_{\mathrm{HC}} & -m_{\mathrm{UA}} & -m_{\mathrm{UP}}\\ -m_{\mathrm{UA}} & m_{\mathrm{AC}} & -m_{\mathrm{CC}}\\ -m_{\mathrm{UP}} & -m_{\mathrm{CC}} & m_{\mathrm{PC}}\end{bmatrix}\ , \tag{3.11}$$

$$\mathbf{C}^{\mathrm{e}}=\begin{bmatrix}c_{\mathrm{HC}} & -c_{\mathrm{UA}} & -c_{\mathrm{UP}}\\ -c_{\mathrm{UA}} & c_{\mathrm{AC}} & -c_{\mathrm{CC}}\\ -c_{\mathrm{UP}} & -c_{\mathrm{CC}} & c_{\mathrm{PC}}\end{bmatrix}\ , \tag{3.12}$$

and

$$\mathbf{K}^{\mathrm{e}}=\begin{bmatrix}k_{\mathrm{HC}} & -k_{\mathrm{UA}} & -k_{\mathrm{UP}}\\ -k_{\mathrm{UA}} & k_{\mathrm{AC}} & -k_{\mathrm{CC}}\\ -k_{\mathrm{UP}} & -k_{\mathrm{CC}} & k_{\mathrm{PC}}\end{bmatrix}\ . \tag{3.13}$$

Elements of these matrices are computed using Eqs. (3.2)–(3.4). Note that the stiffness matrix is zero if the endolymph is modeled as an ideal Newtonian fluid. The forcing vector is

$$\vec{F}^{\mathrm{e}}=\begin{bmatrix}-f_{\mathrm{HC}}-f_{\mathrm{UA}}-f_{\mathrm{UP}}\\ -f_{\mathrm{AC}}-f_{\mathrm{CC}}+f_{\mathrm{UA}}\\ -f_{\mathrm{PC}}+f_{\mathrm{CC}}+f_{\mathrm{UP}}\end{bmatrix}\ . \tag{3.14}$$

4 Model for the cupulae

Equation (3.8) relates the volume displacements of endolymph in the three canals to prescribed head movements and pressure gradients across the three cupulae. To close the system, we must also specify a model for the cupulae. In most previous models of semicircular canal mechanics it was assumed that the cupulae were simple elastic structures (Steinhausen 1933; Buskirk et al. 1976; Oman et al. 1987) or visco-elastic structures (Rabbitt et al. 1994, 1998). These models further assume that cupulae are impermeable to endolymph. The ultrastructure of the cupula is not completely consistent with this type of model. The cupulae are porous and consist of hydrated mucopolysacharide gels containing oriented fiber networks (Hillman 1974; Silver et al. 1997). Damiano (1997, 1999) attempted to incorporate the poro-elastic material behavior of the cupula using bi-phasic mixture theory. In this theory, the cupula was modeled as consisting of a fluid phase and a solid phase, each of which occupies a certain volume fraction of the space (Craine et al. 1970; Browen 1976; Mow et al. 1984). We follow a similar approach here by relating the volume displacement of the solid-matrix phase of each cupula to the corresponding interaction pressure gradient using

$$\mathbf{M}^{\mathrm{c}}\frac{\mathrm{d}^2\vec{Q}^{\mathrm{c}}}{\mathrm{d}t^2}+\mathbf{C}^{\mathrm{c}}\frac{\mathrm{d}\vec{Q}^{\mathrm{c}}}{\mathrm{d}t}+\mathbf{K}^{\mathrm{c}}\vec{Q}^{\mathrm{c}}=\Delta\vec{P}+\vec{F}^{\mathrm{c}}\ , \tag{4.15}$$

where $\mathbf{M}^{\mathrm{c}}$, $\mathbf{K}^{\mathrm{c}}$ and $\mathbf{C}^{\mathrm{c}}$ are diagonal and contain the equivalent mass, stiffness and viscosity of the HC, AC and PC cupulae. The individual elements are again calculated from Eqs. (3.2)– (3.4) but using the effective density $\rho\rightarrow\rho^{\mathrm{c}}$, viscosity $\mu\rightarrow\mu^{\mathrm{c}}$ and shear stiffness $\gamma\rightarrow\gamma^{\mathrm{c}}$ of the cupula. $\vec{F}^{\mathrm{c}}$ is the inertial forcing due to the mass of each cupulae and is computed using Eq. (3.6) where ρ is the total density including both the fluid and solid constituents. The integrations in Eqs. (3.2)–(3.6) are carried out through the thickness, h^{c} of each cupula. $\Delta\vec{P}$ is the interaction force between the solid-cupular matrix and the endolymph. This interaction force is assumed to be proportional to the relative velocities of the fluid phase and the solid phase according to Darcy's law such that the pressure gradient across the cupula is

$$\Delta\vec{P}=\Gamma\left(\frac{\mathrm{d}\vec{Q}^{\mathrm{e}}}{\mathrm{d}t}-\frac{\mathrm{d}\vec{Q}^{\mathrm{c}}}{\mathrm{d}t}\right)\ . \tag{4.16}$$

This pressure gradient appears in the momentum equations for the cupulae (4.15) and the endolymph (3.8) and couples the volume displacement of the cupulae to that of the endolymph. In Eq. (4.16), Γ is inversely related to Darcy's constant D_{a}, the solid-matrix volume fraction ψ, and the cupular cross-sectional area A^{c}, according to $\Gamma=(D_{\mathrm{a}}\psi A^{\mathrm{c}})^{-1}$.

5 Coupled three-canal model

Combining Eq. (3.8) describing endolymph fluid mechanics, Eq. (4.15) describing the visco-elastic response

of the solid phase of the cupula, and Eq. (4.16) describing the interaction between the endolymph and the solid phase of the cupula we find

$$\mathbf{M}\frac{\mathrm{d}^2\vec{Q}}{\mathrm{d}t^2}+\mathbf{C}\frac{\mathrm{d}\vec{Q}}{\mathrm{d}t}+\mathbf{K}\vec{Q}=\vec{F}\ . \tag{5.17}$$

The dependent variables are the endolymph volume flows in each canal and the cupular volume displacements according to

$$\vec{Q}=\begin{bmatrix}\vec{Q}^{\mathrm{e}}\\ \vec{Q}^{\mathrm{c}}\end{bmatrix}\ . \tag{5.18}$$

The mass, stiffness and damping matrices are

$$\mathbf{M}=\begin{bmatrix}\mathbf{M}^{\mathrm{e}} & 0\\ 0 & \mathbf{M}^{\mathrm{c}}\end{bmatrix}\ , \tag{5.19}$$

$$\mathbf{C}=\begin{bmatrix}\mathbf{C}^{\mathrm{e}}+\boldsymbol{\Gamma} & -\boldsymbol{\Gamma}\\ -\boldsymbol{\Gamma} & \mathbf{C}^{\mathrm{c}}+\boldsymbol{\Gamma}\end{bmatrix}\ , \tag{5.20}$$

where $\boldsymbol{\Gamma}=\Gamma\mathbf{I}$, and

$$\mathbf{K}=\begin{bmatrix}\mathbf{K}^{\mathrm{e}} & 0\\ 0 & \mathbf{K}^{\mathrm{c}}\end{bmatrix}\ . \tag{5.21}$$

The first three rows of the inertial forcing vector are associated with the endolymph and the second three rows with the cupulae following

$$\vec{F}=\begin{bmatrix}\vec{F}^{\mathrm{e}}\\ \vec{F}^{\mathrm{c}}\end{bmatrix}\ . \tag{5.22}$$

For the special case of impermeable cupulae, $\Gamma\to\infty$ and the cupular and endolymphatic volume displacements become identical for each canal. In this case, Eq. (5.17) reduce to a set of three equations for $\vec{Q}\to\vec{Q}^{\mathrm{c}}$ (or $\vec{Q}^{\mathrm{e}}$) with $\mathbf{M}\to\mathbf{M}^{\mathrm{e}}+\mathbf{M}^{\mathrm{c}}$, $\mathbf{C}\to\mathbf{C}^{\mathrm{e}}+\mathbf{C}^{\mathrm{c}}$, $\mathbf{K}\to\mathbf{K}^{\mathrm{e}}+\mathbf{K}^{\mathrm{c}}$ and $\vec{F}\to\vec{F}^{\mathrm{e}}+\vec{F}^{\mathrm{c}}$.

As noted above, it is sufficient to use Eq. (3.6) rather than Eq. (3.5). This is confirmed by the form of Eq. (5.22). Substitution of Eq. (3.5) into any row of Eq. (5.22) results in an integral around a closed contour. The integrand for the case of linear acceleration is a constant, hence the contour integral evaluates to zero by Stokes' theorem. The centripetal term also evaluates to zero by application of Stokes' theorem. This proof also requires one to apply the triple-product rule to convert the cross products to inner products, and to note that the labyrinth moves as a rigid body rendering the gradient terms equal to zero.

6 Rotational eigendirections

Eq. (5.17) is a set of six, coupled, second-order differential equations. These equations are particularly simple in that all three matrices **M**, **C** and **K**, are symmetric. The behavior of the system in response to head movements is characterized by the solution of the homogeneous equations, the eigenproblem. Solution of the eigenproblem is facilitated by recasting the equations into Hamilton's canonical form as

$$\mathbf{C}^{\star}\frac{\mathrm{d}\vec{Q}^{\star}}{\mathrm{d}t}+\mathbf{K}^{\star}\vec{Q}^{\star}=\vec{F}^{\star}\ , \tag{6.23}$$

where $\vec{Q}^{\star}$ is a 12-element vector containing the cupulae volume displacements, endolymph volume displacements and corresponding velocities as

$$\vec{Q}^{\star}=\begin{bmatrix}\frac{\mathrm{d}\vec{Q}}{\mathrm{d}t}\\ \vec{Q}\end{bmatrix}\ , \tag{6.24}$$

The symmetric $\mathbf{C}^{\star}$ and $\mathbf{K}^{\star}$ matrices are

$$\mathbf{C}^{\star}=\begin{bmatrix}0 & \mathbf{M}\\ \mathbf{M} & \mathbf{C}\end{bmatrix}\ , \tag{6.25}$$

and

$$\mathbf{K}^{\star}=\begin{bmatrix}-\mathbf{M} & 0\\ 0 & \mathbf{K}\end{bmatrix}\ . \tag{6.26}$$

The forcing vector $\vec{F}^{\star}$ is

$$\vec{F}^{\star}=\begin{bmatrix}\vec{0}\\ \vec{F}\end{bmatrix}\ . \tag{6.27}$$

Considering the transient response, the solution to the homogeneous version of Eq. (6.23) is $\vec{Q}^{\star}=\vec{E}\mathrm{e}^{\alpha t}$. This yields the eigenproblem $[\mathbf{D}+\alpha\mathbf{I}]\vec{E}=\vec{0}$, where the dynamical matrix $\mathbf{D}=\left(\mathbf{C}^{\star-1}\mathbf{K}^{\star}\right)$. The transient part of the solution can be written as a sum of eigenmodes such that

$$\vec{Q}^{\star}=\sum_{j=1}^{6}\vec{E}_j^{\star}\mathrm{e}^{\alpha_j t}\ . \tag{6.28}$$

It will be shown in the Sect. 7 that the system is overdamped such that all 12 of the eigenvalues are real valued negative numbers. A transient head movement will therefore generate cupulae displacements that decay in time as a sum of 12 time constants.

A natural question is, are there any special head movements that excite only one of the eigenmodes and thereby evoke only one time constant and synchronize the temporal response of all three cupulae? To answer this, we consider the forced system and employ an eigenvector expansion of the form

$$\vec{Q}^{\star}=\sum_{j=1}^{6}\vec{E}_j^{\star}T_j(t)\ , \tag{6.29}$$

Substituting this into Eq. (6.23), we find that the time response of the ith mode is governed by

$$\left(\vec{E}_i^{\star T}\mathbf{C}^{\star}\vec{E}_i^{\star}\right)\frac{\mathrm{d}T_i}{\mathrm{d}t}+\left(\vec{E}_i^{\star T}\mathbf{K}^{\star}\vec{E}_i^{\star}\right)T_i=\left(\vec{E}_i^{\star T}\vec{F}^{\star}\right)\ , \tag{6.30}$$

where we have taken advantage of orthogonality of the eigenvectors with respect to $\mathbf{C}^{\star}$, $\mathbf{K}^{\star}$ and $\mathbf{D}^{\star}$. Since the eigenvectors form a complete basis, we can also expand

the forcing $\vec{F}^{\star}(t) = \sum_{j=1}^{6} \mathbf{D}^{\star}\vec{E}_j^{\star}\psi_j(t)$. Substitution into Eq. (6.30) shows that we can excite only the αth mode by selecting a forcing vector of the form $\vec{F}_{\alpha}^{\star} = \mathbf{D}^{\star}\vec{E}_{\alpha}^{\star}\psi_{\alpha}(t)$. To determine if a single eigenmode can be excited by pure rotational head movements, consider three independent rotations about the ground-fixed unit base vectors $\hat{n}_1$, $\hat{n}_2$ and $\hat{n}_3$. From this, apply Eqs. (3.6) and (6.27) to compute $\vec{F}_1^{\star}$, $\vec{F}_2^{\star}$ and $\vec{F}_3^{\star}$ corresponding to identical temporal rotations $\phi(t)$ about three different base vectors. Once these values are computed the forcing vector for an arbitrary rotation about another axis $\hat{n}$ is simply

$$\vec{F}^{\star} = \left[\vec{F}_1^{\star}, \vec{F}_2^{\star}, \vec{F}_3^{\star}\right]\hat{n}\phi(t) \tag{6.31}$$

$$= \mathbf{J}^{\star}\hat{n}_{\alpha}\phi(t) \ , \tag{6.32}$$

where the matrix $\mathbf{J}^{\star} = \left[\vec{F}_1^{\star}, \vec{F}_2^{\star}, \vec{F}_3^{\star}\right]$. Only the αth eigenmode will be excited by the movement if the direction of head rotation $\hat{n}_{\alpha}$ is related to the eigendirection according to

$$\mathbf{J}^{\star}\hat{n}_{\alpha} \propto \mathbf{D}^{\star}\vec{E}_{\alpha}^{\star} \ . \tag{6.33}$$

This system of equations is overdetermined since the vector $\hat{n}_{\alpha}$ has dimensions 1×3 and the vector $\vec{E}_{\alpha}^{\star}$ has dimensions 1×12. Hence, in the general case, it is not possible to prescribe a unidirectional head rotation that excites only one eigenmode of the labyrinth. There are directions, however, that primarily excite one eigenmode. To estimate the relative fraction of energy represented by eigenmode α following a transient excitation, we take advantage of the eigenvector expansion to write

$$\chi_{\alpha} = \frac{\left|\frac{\vec{E}_{\alpha}^{\star}\mathbf{J}^{\star}\hat{n}}{\vec{E}_{\alpha}^{\star}\mathbf{D}^{\star}\vec{E}_{\alpha}}\right|}{\sum_{j=1}^{12}\left|\frac{\vec{E}_j^{\star}\mathbf{J}^{\star}\hat{n}_{\alpha}}{\vec{E}_j^{\star}\mathbf{D}^{\star}\hat{n}}\right|} \ . \tag{6.34}$$

where $\hat{n}$ is a unit vector in the direction of rotation. If $\chi_{\alpha} = 1$ then the eigenmode α would be excited alone, but if $\chi_{\alpha} = 0$ then eigenmode α would not be excited at all. As reported below, we find that some rotational directions excite primarily one eigenmode. The possible significance of this is discussed following presentation of numerical results.

7 Numerical results

7.1 Parameter studies

Simulations were carried out for a number of parameter sets to gain some insight into the behavior of the model. The 3D labyrinthine geometry and the physical properties of the endolymph are relatively well known and were considered fixed in the present simulations (Money et al. 1966; Steer et al. 1967; Money et al. 1971; Buskirk et al. 1976; Oman et al. 1987; Damiano and Rabbitt 1966; Ghanem et al. 1998). The base parameter set is listed in the Appendix. To compute the response of cupulae, a specific head movement must also be specified. Figure 2 provides the HC cupular volume displacement in the form of Bode plots relative to sinusoidal angular head velocity in the anatomical HC plane (gain, $\mathrm{pl}\cdot{}^{\circ -1}\cdot\mathrm{s}$; phase, deg, re: peak head velocity). Keeping with the established convention in vestibular physiology, a phase of 0°corresponds to peak head velocity, a phase of +90° corresponds to peak head acceleration, and a phase of −90° corresponds to peak head displacement. Cupular stiffness and porosity as well endolymph stiffness and duct size were studied. In almost all cases considered, the gain was relatively flat and the phase was near zero over a majority of the physiological range of angular head frequencies (0.01–10 Hz). The model predicted a decrease in gain and an increase in phase at low frequencies and, typically, a decrease in gain and phase at high frequencies. Figure 2A illustrates shifts in the lower-corner resulting from changes in the cupular elastic shear modulus γ^c. Solid curves are for moduli ranging from 10 times less than the baseline to 10 times greater than the baseline. As expected from Eq. (3.4), the inverse trend was observed for changes in ampulla size (or cupular area, not shown). Increasing porosity of the cupula also shifted the lower corner to higher frequen-

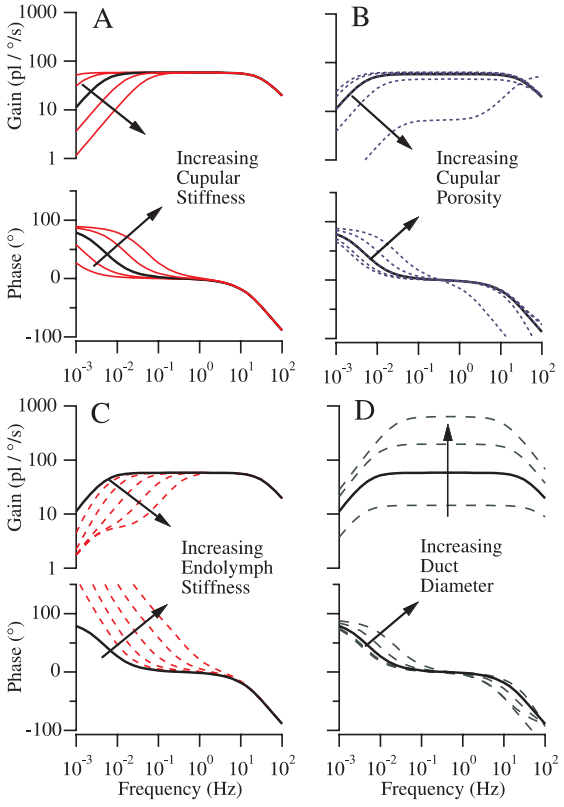

Fig. 2A–D. Single canal parameter study. The influence of changing the elastic modulus (**A**, *thin solid curves*) and Darcy's constant (**B**, *short dashed curves*) of the cupulae on the volume displacement of the HC cupula (Gain, $\mathrm{pl}\cdot\mathrm{deg}^{-1}\mathrm{s}^{-1}$, Phase, deg. re, peak head velocity) are shown for rotation in the HC plane. Results are shown relative to the baseline parameters (*thick solid curves*). *Lower panels* show the influence of adding stiffness to the endolymph (**C**, *dashed curves*) and changing the diameter of the membranous ducts (**D**, *long dashed curves*)

cies, but porosity had the additional influence of decreasing the midband gain and altering the behavior of the upper corner (short dashed curves, Fig. 2B). The endolymph was assumed to be Newtonian, having zero shear stiffness with the exception of example results in Fig. 2C. Results show the influence of increasing the endolymphatic stiffness γ^e from a level 100× less than that of the cupula to a level 10 times less than the cupula. Simulations indicate that even a very small endolymphatic stiffness could significantly alter the low frequency response. Endolymphatic stiffness has not yet been measured and hence was assumed to be zero in all but the example simulations in Fig. 2C. Decreasing the cross-sectional dimensions of the labyrinthine ducts by a factor of 10 without changing the ampullary dimensions, decreased the gain and increased the bandwidth (Fig. 2D). Changing the radius of the toroid without changing the cross-sectional area had relatively little effect on the dynamics due to the additional inertial force being offset primarily by additional viscous drag (not shown). The results (Fig. 2) for the HC computed using the three-canal model agree quite well with predictions of single-canal models reported previously (Oman et al. 1987; Damino and Rabbitt 1996; Damiano 1997; Rabbitt et al. 1998). This provides an important consistency check between the current three-canal model and previous single-canal models.

7.2 Maximal response directions

The advantage of the three-canal model over single-canal models is that it allows for direct investigation of directional coding. Of most interest are changes in response to dynamics associated with various directions of head rotation. Specific numerical results are provided here for the right labyrinth undergoing rotations about fixed axes. The model predicts a maximal response direction (denoted $\hat{n}^{\max}$) for each canal. Rotation about this special axis maximizes the volume displacement of the respective cupula. In accordance with this, rotation about any axis orthogonal to $\hat{n}^{\max}$ nulls the cupular volume displacement. The set of vectors perpendicular to $\hat{n}^{\max}$ define the null plane of the particular canal. Null planes have been used previously to experimentally determine maximal response directions (Estes et al. 1975; Reisine et al. 1988; Dickman 1996). The gain of the HC cupula is illustrated in Fig. 3 as a function of direction of canal rotation. Results vary slightly with frequency as indicated below and are shown in Fig. 3 for rotation at 1 Hz. The response is well described by a cosine rule. In Fig. 3A, θ corresponds to the angle between a vector along the maximal response direction and the axis of head rotation. A vector drawn from the center of rotation (origin in Fig. 3B–E) to the circle (Fig. 3B; sphere in Fig. 3C–E) provides the gain for a head rotation about the particular axis. Fig. 3C–E where the bubbles provide 3D versions for the HC, AC and PC, respectively. The maximal response direction is predicted for rotations about the long axis of the double bubble. The corresponding minimal response plane is

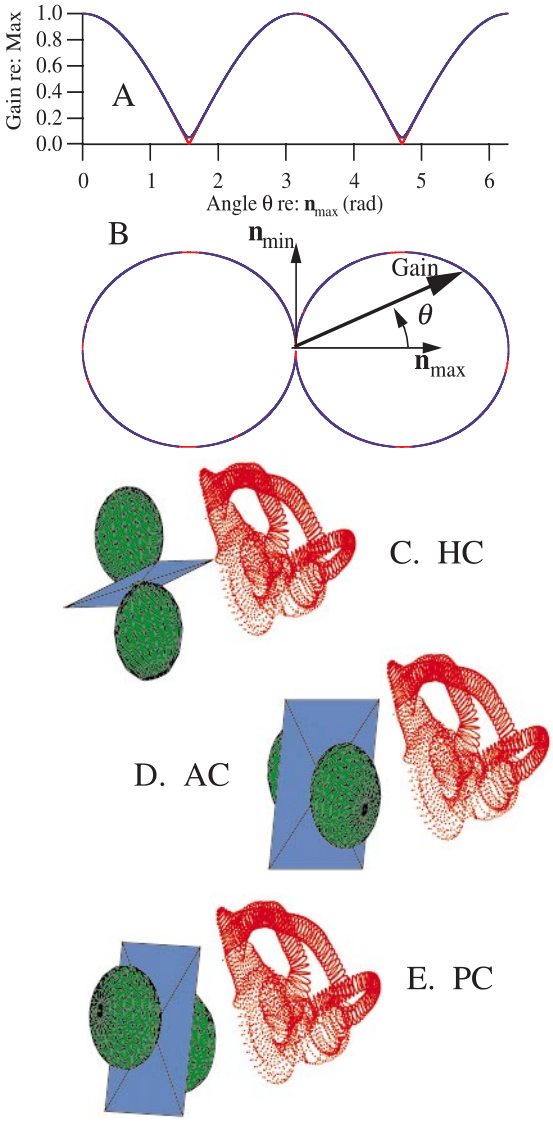

Fig. 3A–E. Maximal response directions. **A** and **B** show cupular volume displacement gain as a function of angle θ from the maximal response direction. Results are normalized to a peak gain of one. In **B** the length of the vector from the origin to the *solid circular bubbles* provides the relative gain. Directional sensitivities of the HC, AC and PC differ only in the direction of maximal response $\hat{n}_{\max}$. Three-dimensional response bubbles are shown in **C**, **D** and **E** for the HC, AC and PC, respectively. Results are shown relative to wire-frame reconstructions of the labyrinth from a caudal viewpoint. Null planes for each canal are indicated as gray surfaces passing directly between the response bubbles

perpendicular to the maximal response direction (grey square). Orthographic projections are shown in Fig. 4 along with the centerlines of the HC (solid), AC (short dashed) and PC (long dashed).

7.3 Geometrical canal planes

Anatomical canal planes were determined by minimizing the squared distance between the centerline of each

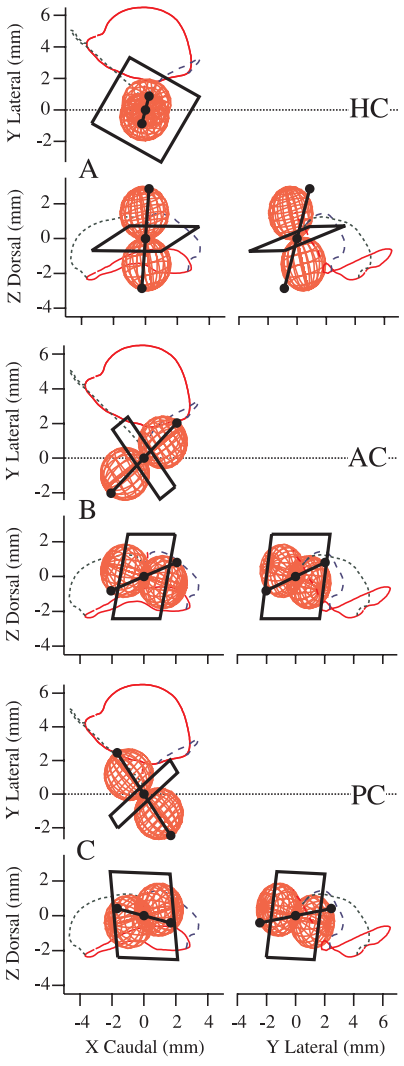

Fig. 4. Orthographic projections of maximal response directions. Null planes (*thick squares*) and maximal response directions (*wire-frame bubbles*) and prime directions (*thick solid lines* terminated by *solid circles*) are shown in three orthogonal views for the HC (**A**), AC (**B**) and PC (**C**). The prime directions are the rotational directions that null two canals while maintaining a relatively large gain in the the prime canal. Notice that the prime directions are not identical to the maximal response directions

slender duct and flat planes. Unit normal vectors perpendicular to these geometrical canal planes are provided in Table 1 for the HC, AC and PC (denoted $\hat{n}^{\text{geom}}$). Results are reported relative to the head-fixed coordinate system illustrated in Figs. 1, 3 and 4. In the case of the HC, the maximal direction and a normal vector perpendicular to the geometrical canal plane differ by $\approx 8.8°$. The AC and PC show differences of $\approx 16.8°$ and $\approx 3.8°$, respectively. Differences between the anatomical normal vectors and maximal response directions result primarily from fluid coupling between the three canals in the model. These results were determined using anatomical canal planes derived from the slender portion of each canal. If we also include the common crus and utricular segment in the computation, the difference between anatomical and maximal response

Table 1. Unit normal vectors

Normal vector	X	Y	Z
$\hat{n}^{\text{max}}_{\text{HC}}$	0.044	0.284	−0.958
$\hat{n}^{\text{geom}}_{\text{HC}}$	0.155	0.380	−0.912
$\hat{n}'_{\text{HC}}$	−0.024	−0.306	−0.952
$\hat{n}^{\text{max}}_{\text{AC}}$	−0.775	−0.596	0.212
$\hat{n}^{\text{geom}}_{\text{AC}}$	−0.676	−0.736	−0.025
$\hat{n}'_{\text{AC}}$	−0.723	−0.653	−0.227
$\hat{n}^{\text{max}}_{\text{PC}}$	−0.613	0.757	−0.228
$\hat{n}^{\text{geom}}_{\text{PC}}$	−0.651	0.713	−0.262
$\hat{n}'_{\text{PC}}$	−0.559	0.802	0.212

directions is even greater on average. Hence, anatomical canal planes, regardless of computation technique, are predicted to be relatively crude indicators of the maximal response directions of individual canals.

Maximal response directions are predicted to vary slightly with the frequency of head oscillation. The average angle between the maximal response direction and the anatomical canal direction is $8.67° + -0.67°$SD for the HC, $17.0° + -0.72°$SD for the AC and $3.98° + -0.34°$SD for the PC. Averaging all results (0.001–100Hz, three canals), the model predicts an average difference of 9.9° between anatomical canal planes and the directions of maximal response. This prediction falls well within the range of the data reported for other species (Estes et al. 1975; Reisine et al. 1988; Dickman 1996). A summary showing anatomical canal directions and maximal response directions is provided for 1 Hz rotational stimulation in Fig. 6. Results are shown graphically in orthographic projection form based on the data in Table 1. These data were used to compute angles between maximal response directions, geometric response directions, and prime response directions. Angles between these vectors are summarized in Table 2.

7.4 Prime directions

The model also predicts that rotation about a maximal response direction $\hat{n}^{\text{max}}$ of one canal does not minimize

Table 2. Euler angles

Vector 1	Vector 2	Euler Angle (°)
$\hat{n}^{\text{max}}_{\text{HC}}$	$\hat{n}^{\text{geom}}_{\text{HC}}$	8.8
$\hat{n}^{\text{max}}_{\text{HC}}$	$\hat{n}'_{\text{HC}}$	41.6
$\hat{n}^{\text{geom}}_{\text{HC}}$	$\hat{n}'_{\text{HC}}$	34.6
$\hat{n}^{\text{max}}_{\text{AC}}$	$\hat{n}^{\text{geom}}_{\text{AC}}$	16.8
$\hat{n}^{\text{max}}_{\text{AC}}$	$\hat{n}'_{\text{AC}}$	12.8
$\hat{n}^{\text{geom}}_{\text{AC}}$	$\hat{n}'_{\text{AC}}$	25.7
$\hat{n}^{\text{max}}_{\text{PC}}$	$\hat{n}^{\text{geom}}_{\text{PC}}$	3.8
$\hat{n}^{\text{max}}_{\text{PC}}$	$\hat{n}'_{\text{PC}}$	28.4
$\hat{n}^{\text{geom}}_{\text{PC}}$	$\hat{n}'_{\text{PC}}$	25.8
$\hat{n}'_{\text{HC}}$	$\hat{n}'_{\text{AC}}$	64.3
$\hat{n}'_{\text{HC}}$	$\hat{n}'_{\text{PC}}$	115.7
$\hat{n}'_{\text{AC}}$	$\hat{n}'_{\text{PC}}$	99.7

the response of the two sister canals. Consider the response of the AC and PC illustrated in Fig. 4. Null response planes for the AC and PC lie perpendicular to the maximal response directions sandwiched between the response bubbles. These two planes intersect along a line denoted, $\hat{n}'_{HC}$, the prime direction of the HC. Rotation about this direction simultaneously nulls the response of the AC and the PC while maintaining a large HC gain. There are three such directions for each labyrinth, one direction associated with each canal. Orientations of the prime directions are illustrated relative to maximal response directions in Fig. 4, and relative to each other in Fig. 5. Numerical values are listed in Table 1. The prime directions differ from the maximal response directions and from the anatomical canal planes, in this model geometry, by an average of 28° and 29°, respectively. It is significant to note that rotation about a prime direction is predicted to excite only one canal nerve. For general 3D angular movements, the model predicts that the motion is decomposed into base vectorial components in the prime directions. Each of these components is predicted to be carried by a single canal nerve. As for the maximal response directions, the prime directions are predicted to vary slightly with stimulus frequency. The average angle between the prime response direction and the anatomical canal normal vector is $41.6° + -0.13°$SD for the HC, $13.0° + -0.65°$SD for the AC and $28.3° + -1.05°$SD for the PC.

7.5 Three-canal response

Figure 7 provides Bode plots for the HC, AC and PC for rotations about three different axes associated with the AC. Graphs on the left provide the gain and phase of

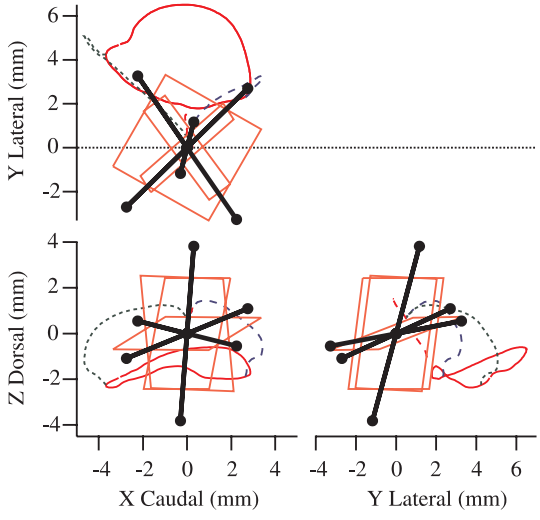

Fig. 5. Prime directions. The prime directions (*thick solid lines* terminated with circles) and null planes (*squares*) from Fig. 4 are replotted in orthographic views to illustrate their relative orientations. The model predicts that the canals decompose 3D angular motions into vectoral components along these prime directions, one associated with each canal nerve

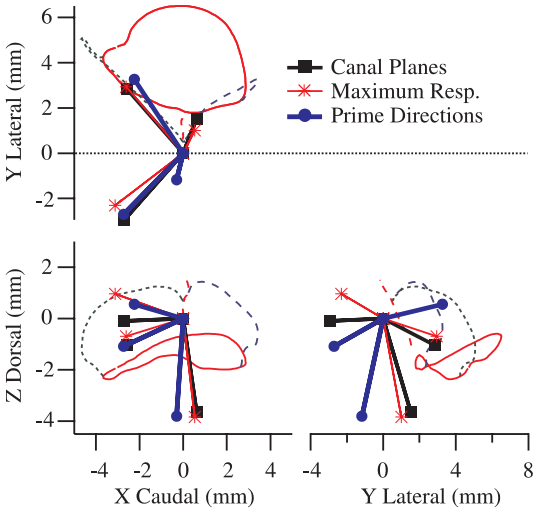

Fig. 6. Comparison of anatomical and physiological directions. Orthographic projections of vectors along the maximal response directions, prime directions, and anatomical canal plane normals are shown. Prime response directions do not align with the maximal response directions or anatomical directions in any canal

cupular volume displacement relative to head rotational velocity. Graphs on the right provide the corresponding gain and phase of endolymphatic volume displacement in the ampullae. Endolymphatic volume displacements are not identical to cupular displacements due to slight porosity of the cupulae. The porosity alters the volume displacement of the cupula primarily at low frequencies. The top panels in Fig. 7A provide results for head rotations about the AC maximal response direction $\hat{n}^{max}_{AC}$. Center panels (Fig. 7B) are for rotations about a normal vector perpendicular to the AC anatomical canal plane $\hat{n}^{geom}_{AC}$. Notice that the PC response is reduced when rotating in the AC anatomical canal plane relative to rotating about the AC maximal response direction. Lower panels (Fig. 7C) show results for rotations about the AC prime direction, $\hat{n}'_{AC}$, which maximizes the cupular volume displacement in the AC relative to the HC and PC. In C, both the PC and HC responses are greatly reduced while the response of the AC is nearly maximal. The prime and maximal response directions were computed at 1 Hz and held fixed to generate the Bode plots. As a result, the HC and PC nulls in Fig. 7 are nearly perfect only at 1 Hz. Even without including the frequency-dependence of the null plane, the HC and PC responses are down by ≈100 relative to the AC. This is not the case for rotations about the maximal response direction (Fig. 7A) or the anatomical canal plane (Fig. 7B).

7.6 Eigenvalues and eigenvectors

The solution of the eigenproblem provides 12 real-valued eigenvalues α_n and 12 corresponding eigenvectors $\vec{E}_n$. Three of the eigenvalues are zero for the particular parameter set used in this study. This would not be the

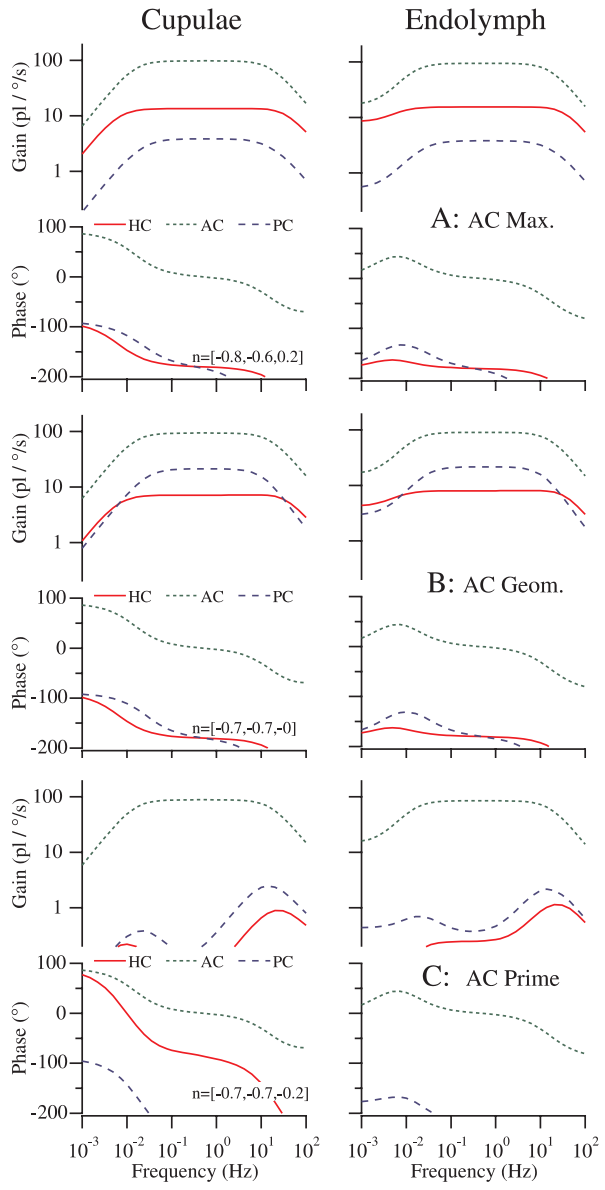

Fig. 7A–C. Dynamic response of the AC cupula and endolymph. AC Bode plots providing the volume displacement of the AC cupula are provided on the left and the corresponding Bode plots for volume displacement of endolymph in the AC ampulla are provided on the right. The *top graphs* (**A**) are for rotation about the axis which maximizes the AC cupular gain. *Center graphs* (**B**) are for rotation in the anatomical canal plane, and *lower graphs* (**C**) are for rotation about the AC prime response direction. The direction of rotation is indicated in the legend as $n = [,,]$. Notice that there is very little difference between the peak AC gain for rotation about any of the three directions, but the HC and PC gains are highly attenuated for rotation about the prime direction. The same trend follows for endolymph displacement. Endolymph and cupular volume displacements are not identical due to porosity of the cupula

case for a non-zero endolymphatic stiffness. The nine non-zero eigenfrequencies are $\alpha \in (0.0064, 0.015, 0.029, 12.28, 16{,}56, 33.95, 4060, 4088, 4129)$ Hz. The first six eigenfrequencies correspond roughly to upper and lower corner frequencies of traditional single-canal models (Oman et al. 1987), but in the three-canal model they are not affiliated with only one canal. These six frequencies correspond to time constants ranging over 0.0047–24.9 s. The values 0.0064, 0.015 and 0.029 Hz correspond to the lower corners and are primarily responsible for the attenuation in gain and upswing in phase at low frequencies (Fig. 7). The values 12.28, 16.56 and 33.95 Hz correspond to the upper-corners and are primarily responsible for the attenuation in cupular gain and roll-off in phase at high frequencies.

As described in the analysis above, the solution during head rotation can be written using an eigenvector expansion. Analytical results show, in general, that it is not possible to excite exactly one eigenmode by a pure head rotation about a single axis. Hence, one would expect multiple time constants to be present in the dynamic response of each cupula. For some rotational directions, however, it appears that the system responds primarily in one eigenmode. Of special interest are the prime directions $\hat{n}'$ which represent the natural coordinates of the labyrinth. Substitution of each of these vectors into Eq. (6.34) shows that the three lowest eigenmodes are dominant. For rotation about the HC prime direction, $\hat{n}'_{\mathrm{HC}}$, 98% of the response is in mode 1 (eigenfrequency 0.0064 Hz). For a transient rotation about the AC prime direction, $\hat{n}'_{\mathrm{AC}}$, 97% of the response is in mode 2 (eigenfrequency 0.015 Hz). For rotation about the PC prime direction, $\hat{n}'_{\mathrm{PC}}$, 93% of the response is in mode 3 (eigenfrequency 0.029 Hz). Hence, the transient response is predicted to be dominated by three eigenmodes and three eigenvectors regardless of rotational direction. This indicates that three time constants, one associated with each prime direction, may be adequate to describe the macromechanical response of the labyrinth.

8 Discussion

Results show the existence of maximal and prime directions that are distinct from each other and from anatomical canal directions. Differences between maximal, anatomical and prime directions are predicted by the model to be a direct result of three-canal macromechanics. There are two features that underlie these predictions. The first is the fact that individual canals are not perfect toroids and do not lie in perfectly flat planes (Oman et al. 1987). The other, more salient, feature is fluid coupling between the canals. Endolymph flow in one canal entrains fluid movement in the sister canals owing to shared fluid in the utricular vestibule and common crus (Muller and Verhagen 1988a, b). Multi-canal interactions are facilitated by adverse pressure gradients, which have been predicted to be particularly large near canal bifurcation points (Rabbitt et al. 1998). These effects shift the maximal response directions away from the canal planes.

It is straightforward, and mathematically valid, to decompose a head rotation into any of the three canonical sets of basis vectors – maximal, prime or anatomical. The question is which decomposition, if any, is carried out by the semicircular canals? If we consider a

rotation about a maximal response direction of any given canal, all three canal nerves are predicted to respond. The system decomposes this rotation into three components, one carried in each canal nerve. Hence, head rotations are not resolved into components along maximal response directions. The same finding holds for rotation about anatomical canal planes. In contrast, if we rotate about a prime direction all of the neural response is predicted to be isolated to a single canal nerve. This is consistent with directional sensitivities observed in afferent nerves (Estes et al. 1975; Reisine et al. 1988; Dickman 1996). Therefore, the semicircular canals resolve angular head movements into vectorial components along the prime directions. These directions can be determined from experimental data, or estimated using a model, by intersecting null planes for two canals. The intersection defines a line which runs along the prime direction for the third canal (Fig. 5).

Sensitivity of each canal in the present model obeys a simple cosine rule. This means that a 20° deviation from the maximal response direction causes only a 6% decline in gain from the maximum value. The same 20° deviation from a null plane causes the gain to recover 34% of its maximum value. Hence, the null planes show a much sharper spatial tuning than the maximal response directions. The prime directions show the same sharp tuning as the null planes.

Results suggest a very simple model to describe how the semicircular canals decompose angular head movements into separate vectorial components carried by each canal nerve. The 3D angular acceleration of the head, $\vec{\Omega}$, written in terms of unit vectors in the prime directions is

$$\ddot{\vec{\Omega}} = \ddot{\Omega}_{\mathrm{HC}}\hat{n}'_{\mathrm{HC}} + \ddot{\Omega}_{\mathrm{AC}}\hat{n}'_{\mathrm{AC}} + \ddot{\Omega}_{\mathrm{PC}}\hat{n}'_{\mathrm{PC}} \ , \tag{8.35}$$

where $\hat{n}'_{\mathrm{HC}}$, $\hat{n}'_{\mathrm{AC}}$ and $\hat{n}'_{\mathrm{PC}}$ are the prime directions, and $\ddot{\Omega}_{\mathrm{HC}}$, $\ddot{\Omega}_{\mathrm{AC}}$ and $\ddot{\Omega}_{\mathrm{PC}}$ are the scalar vectorial components of acceleration which excite each canal separately. This simple equation reproduces all of the directional behavior of the 3D model including maximal response directions and null planes. To use the equation, it is necessary to experimentally determine the prime directions (or estimate the directions using a model such as described above). It is valid only if the base vectors are the prime directions. For example, use of the $\hat{n}^{\max}$ instead of $\hat{n}'$ would require a matrix multiplication, not a simple vectorial addition. In interpreting the components it is important to note that the $\hat{n}'$ unit vectors are non-orthogonal. For an orthogonal set of base vectors, individual components are maximized for a stimulus in the base direction. This is not the case for the non-orthogonal decomposition, which result in a maximum for a stimulus skewed at an angle relative to the base vector.

Equation (8.35) can be applied in one of two ways. The first would be to determine $\ddot{\vec{\Omega}}$ from the components $\ddot{\Omega}_{\mathrm{HC}}$, $\ddot{\Omega}_{\mathrm{AC}}$ and $\ddot{\Omega}_{\mathrm{PC}}$, a task that must be carried out by the brain to reconstruct/represent 3D angular head movements on the basis of individual canal nerve responses. The second application would be to determine how a 3D angular head acceleration is parsed to excite each of the three canals. For this, Eq. (8.35) must be inverted. The result is

$$\begin{bmatrix} \ddot{\Omega}_{\mathrm{HC}} \\ \ddot{\Omega}_{\mathrm{AC}} \\ \ddot{\Omega}_{\mathrm{PC}} \end{bmatrix} = \mathbf{P}^{-1} \begin{bmatrix} \ddot{\vec{\Omega}} \cdot \hat{n}'_{\mathrm{HC}} \\ \ddot{\vec{\Omega}} \cdot \hat{n}'_{\mathrm{AC}} \\ \ddot{\vec{\Omega}} \cdot \hat{n}'_{\mathrm{PC}} \end{bmatrix} \ , \tag{8.36}$$

where $\mathbf{P}$ is the matrix of direction cosines defined by inner products of the prime unit vectors

$$\mathbf{P} = \begin{bmatrix} 1 & \hat{n}'_{\mathrm{AC}} \cdot n'_{\mathrm{HC}} & \hat{n}'_{\mathrm{PC}} \cdot n'_{\mathrm{HC}} \\ \hat{n}'_{\mathrm{HC}} \cdot n'_{\mathrm{AC}} & 1 & \hat{n}'_{\mathrm{PC}} \cdot n'_{\mathrm{AC}} \\ \hat{n}'_{\mathrm{HC}} \cdot n'_{\mathrm{PC}} & \hat{n}'_{\mathrm{AC}} \cdot n'_{\mathrm{PC}} & 1 \end{bmatrix} \ . \tag{8.37}$$

Equation (8.36) embodies the directional decomposition carried out by canal macromechanics. It is important to note that the unit vectors $\hat{n}'$ are defined in the head-fixed system and hence the angular acceleration $\ddot{\vec{\Omega}}_{\mathrm{inertial}}$ must be resolved into the head-fixed system using Eq. (3.7) to obtain $\ddot{\vec{\Omega}}$ prior to application of Eq. (8.35) or Eq. (8.36).

The specific strategy used by the canals to encode the direction of angular movement may be particularly important to function of the VOR. Computations required to control the motion of the eyes in the presence of head movements would be simplified if individual semicircular canal directional sensitivities were aligned closely with the extraocular muscle pulling directions. The anatomy of both lateral-eyed and frontal-eyed animals indicate that only a partial alignment is present and that the alignment is insufficient to account for the established directional accuracy of the VOR (Ezure and Graf 1984a, b; Graf 1988). Models of the VOR therefore postulate the existence of a coordinate system transformation, implemented by the central nervous system, to map weighted canal signals to the appropriate extraocular muscles (Pellionisz and Llinäs 1980; Robinson 1982; Ezure and Graf 1984a; Pellionisz and Graf 1987; Peterson et al. 1992). To determine the weighting, or transformation, it is first necessary to know how the direction of angular movement is decomposed into components carried by each nerve. Present results strongly indicate that this decomposition is according to prime directions, not canal planes or maximal response directions. The relatively large differences predicted between canal planes, maximal response directions and prime response directions indicate that this neural transformation may be somewhat different than previously reported.

It is well established that stimulation of bilateral synergistic ampullary nerves mainly leads to contraction of one agonist-antagonist muscle pair in each eye (Szentágothai 1950; Fluur 1959; Suzuki and Cohen 1964; Cohen et al. 1964; Suzuki et al. 1969; Ito et al. 1973; Ito et al. 1976). Eye movements resulting from stimulation of a single ampullary nerve are slightly more complicated. In cats, for example, stimulation of a single HC ampullary nerve leads mainly to horizontal eye movements in both eyes corresponding to activa-

tion of the medial rectus in the ipsilateral eye and the lateral rectus in the contralateral eye. Stimulation of a single AC nerve leads to upward vertical movement in the ipsilateral eye and torsional rolling in the contralateral eye, while stimulation of a single PC nerve leads to downward movement of the contralateral eye and torsional rolling of the ipsilateral eye (Cohen and Suzuki 1962, 1963). The electrical stimulus used in these studies primarily activates only one ampullary nerve at a time. Hence, the single canal stimulus is nearly equivalent to rotation about one of the prime directions described above (with the contralateral labyrinth inactivated). This correspondence would suggest that rotation about a prime direction of one labyrinth, in the absence of input from the other labyrinth, would lead to the same characteristic eye movements observed during electrical stimulation. Consider rotation about the AC prime direction indicated in Fig. 5. It is interesting to note that $\hat{n}'_{AC}$ appears to align quite well with anatomical directions in the toadfish associated with vertical eye movements in the ipsilateral eye and primarily with torsional movements in the contralateral eye (plus some vertical in the contralateral eye). This alignment is remarkably similar to the physiology reported using electrical stimulation in other species. Analogous correlations hold for the HC and PC. This leads to the hypothesis that the VOR may be centrally organized primarily according to prime directions of the end organs. These prime directions are associated with individual canal nerves, not canal planes or maximal response directions. This hypothesis may be important to the neural representation of 3D angular movements. Future studies should experimentally test of the correspondence between labyrinthine prime directions and the kinematics of the ocular plant, perhaps in a species with a highly developed VOR.

The model also predicts a partial correspondence between the prime directions and eigenvectors of the dynamical system of equations. The eigenmodes of the system play a fundamental role in the transient response and frequency dependence. It was shown above that it is not possible to excite only one eigenmode using head rotation about a single axis. Numerical results, however, indicate that it is possible to feed most of the energy into a single eigenmode for rotations about the prime directions. For complex movements the model would predict the mechanical response to be dominated by three eigenmodes, each of which is primarily associated with a single prime direction and a single canal nerve. The temporal response properties of a single canal cupula would therefore be predicted to be dominated by a single time constant irrespective of the complexity of the angular movement. In addition, the temporal response characteristics of single canal afferents are predicted by the model to be completely insensitive to acceleration components in the sister-canal prime directions.

In closing, there are several limitations to the model that should be noted. The model only addresses fluid and cupular volume displacements and it is not possible to extract detailed cupular displacement fields, stereociliary bundle deflections, or neural responses. The assumption of duct rigidity may not be valid for high accelerations or at frequencies above ≈10 Hz (Rabbitt et al. 1998). This is due to increasing translabyrinthine pressures associated with high accelerations which are believed to cause membranous duct and ampullary distention. We have also assumed Poiseuille flow which gives the velocity-profile factor $\lambda = 8\pi$. This is sufficient below ≈10 Hz but introduces some error at higher frequencies (Damiano and Rabbitt 1996). Although the local cross-sectional area of each of the ducts and ampullae was included, ellipticity was ignored. Ducts of the fish labyrinth are relatively circular in cross-sectional area, so this assumption has no discernable impact on the present results (Ghanem et al. 1998). Application of the model to humans or other species with more elliptical ducts should include the correction factor presented by Oman et al. (1987). The asymptotic solution (Damiano and Rabbitt 1996) used in the present model for the endolymph does not account for local circulation in the ampullae, utricular vestibule or CC. These flows are expected to be small at low frequencies but may have some effect at higher frequencies (Makhijani et al. 1996). Data remain insufficient to quantify the influence of local cross-sectional flows. With regard to the geometry, the model was applied to the reconstructed morphology of the oyster toadfish, *Opsanus tau* (Ghanem et al. 1998). The existence of prime directions certainly extends to other species, but the specific numerical values cannot be extrapolated. Comparison of experimental data to predictions of the present model for various species remains a topic of future work.

Appendix

Numerical values for parameters used in the model are listed in Table 3.

Acknowledgements. Partial support for this work was provided by the National Institutes of Health NIDCD P01-DC01837 and the Center for High Performance Computing at the University of Utah.

Table 3. Parameter values

Parameter	Value	Units
ρ^e	1.0	$g \cdot cm^{-3}$
μ^e	8.5×10^{-3}	$dyn \cdot s^{-1} \cdot cm^{-1}$
γ^e	0	$dyn \cdot cm^{-2}$
ρ^c	1.0	$g \cdot cm^{-3}$
μ^c	0.1	$dyn \cdot s^{-1} \cdot cm^{-1}$
γ^c	2.0×10^{-1}	$dyn \cdot cm^{-2}$
Γ	2.0×10^{5}	$dyn \cdot s^{-1} \cdot cm^{-5}$
A^c	1.0×10^{-2}	cm^2
h^c	8.0×10^{-2}	cm

References

Abend WK (1977) Functional organization of the superior vestibular nucleus of the squirrel monkey. Brain Res 132:65–84

Berthoz A, Grantyn A (1986) Neuronal mechanisms underlying eye-head coordination. In: Freund HJ, Büttner U, Cohen B, Noth J (eds) The oculomotor and skeletal motor systems: differences and similarities. Progress in brain research, vol 64. Elsevier Amsterdam, pp 325–354

Blanks RHI, Estes MS, Markham CH (1975) Physiological characteristics of vestibular first-order neurons in the cat. ii. Response to angular acceleration. J Neurophysiol 38:1250–1268

Blanks RHI, Curthoys IS, Bennett ML, Markham CH (1985) Planar relationships of the semicircular canals in rhesus and squirrel monkeys. Brain Res 340:315–324

Bowen RM (1976) Theory of Mixtures. In: Erigen AE (ed) Continuum physics. Academic Press, New York, pp 1–127

Boyle R, Highstein SM (1990) Resting discharge and response dynamics of horizontal semicircular canal afferents of the toadfish, *Opsanus tau* J Neurosci 10:1557–1569

Brichta AM, Goldberg JM (1996) Afferent and efferent responses from morphological fibers classes in the turtle posterior crista. Ann NY Acad Sci 781:183–195

Buskrik WC, Van Watts RG, Liu YK (1976) The fluid mechanics of the semicircular canals. J Fluid Mech 78:87–98

Cohen B (1988) Representation of three-dimensional space in the vestibular, oculomotor, and visual systems. In: Cohen B, Henn V (eds) Representation of three-dimensional space in the vestibular, oculomotor, and visual systems vol 545. Ann NY Acad Sci, pp 239–247

Cohen B, Suzuki JI (1962) Oculomotor effects of ampullary nerve stimulation. Physiologist 5:119

Cohen B, Suzuki JI (1963) Eye movements induced by ampullary nerve stimulation. Am J Physiol 204:347–351

Cohen B, Suzuki JI, Bender MB (1964) Eye movements from semicircular canal nerve stimulation in the cat. Ann Otol Rhinol Laryngol 73:153–169

Collewijn H (1975) Direction-selective units in the rabbit's nucleus of the optic tract. Brain Res 100:489–508

Craine RE, Green AE, Naghdi PM (1970) A mixture of viscoelastic material with different temperature. Q J Appl Math 23:171–184

Curthoys IS, Markham CH (1971) Convergence of labyrinthine influences on units in the vestibular nuclei in cat. i. Natural stimulation. Brain Res 35:469–490

Damiano ER (1997) A bi-phasic model of the cupula and the low-frequency mechanics of the vestibular semicircular canal. Am Soc Mech Eng Bed 35:61–62

Damiano ER (1999) A poroelastic continuum model of the cupula partition and the response dynamics of the vestibular semicircular canal. ASME J Biomech Eng (in press)

Damiano ER, Rabbitt RD (1996) A singular perturbation model for fluid dynamics in the vestibular semicircular canal and ampulla. J Fluid Mech 307:333–372

Dickman JD (1996) Spatial orientation of semicircular canals and afferent sensitivity vectors in pigeons. Exp Brain Res 111:8–20

Estes MS, Blanks RHI, Markham CH (1975) Physiologic characteristics of vestibular first-order neurons in the cat. i. Response plane determination and resting discharge characteristics. J Neurophysiol 38:1239–1249

Ezure K, Graf W (1984a) A quantitative analysis of the spatial organization of the vestibulo-ocular reflexes in lateral- and frontal-eyed animals. ii. Neuronal networks underlying vestibulo-oculomotor coordination. Neuroscience 12:95–109

Ezure K, Graf W (1984b) A quantitative analysis of the spatial organization of the vestibulo-ocular reflexes in lateral- and frontal-eyed animals. i. Orientation of semicircular canals and extraocular muscles. Neuroscience 12:85–93

Fernández C, Goldberg JM (1971) Physiology of peripheral neurons innervating semicircular canals of the squirrel monkey. ii. Response to sinusoidal stimulation and dynamics of peripheral vestibular system. J Neurophysiol 34:661–675

Fluur E (1959) Influences of semicircular canal ducts on extraocular muscles. Acta Otolaryngol Suppl 149:5–46

Fukushima K, Perlmutter SI, Baker JF, Peterson, BW (1990) Spatial properties of second-order vestibulo-ocular relay neurons in the alert cat. Exp Brain Res 81:462–478

Ghanem TA, Rabbitt RD, Tresco PA (1998) Three-dimensional reconstruction of the membranous vestibular labyrinth in the toadfish, *Opsanus tau*. Hear Res 124:27–43

Goldberg JM, Fernández C (1971) Physiology of peripheral neurons innervationg semicircular cnals of the squirrel monkey. i. Resting discharge and response to constant angular accelerations. J Neurophysiol 34:635–660

Graf W (1988) Motion detection in physical space and its peripheral and central representation. Ann NY Acad Sci 545:154–169

Graf W, Ezure K (1986) Morphology of vertical canal related second order vestibular neurons in the cat. Exp Brain Res 63:35–48

Graf W, McCrea RA, Baker R (1983) Morphology of posterior canal related secondary vestibular neurons in rabbitt and cat. Exp Brain Res 52:125–138

Gray AA (1907) The labyrinth of animals VI. Churchill, London

Gray AA (1908) The labyrinth of animals VII. Churchill, London

Harai N, Uchino Y (1984) Superior vestibular nucleus neurones related to the excitatory vestibulo-ocular reflex of anterior canal origin and their ascending course in the cat. Neurosci Res 1:73–79

Hillman CE (1974) Cupular structure and its receptor relationship. Brain Behav Evol 10:52–68

Hoffmann KP (1982) Cortical vs subcortical contributions to the optokinetic reflex in the cat. In: Lennerstrand G, Zee DS, Keller E (eds) Functional basis of ocular motility disorders. Pergamon Press, Oxford pp 303–310

Hoffmann KP (1988) Responses of single neurons in the pretectum of monkeys to visula stimuli in three-dimensional space. In: Cohen B, Henn V (eds) Representation of three-dimensional space in the vestibular, oculomotor and visual systems, vol 545. Ann NY Acad Sci, pp 180–186

Igarashi M (1967) Dimensional study of the vestibular apparatus. Laryngoscope 77:1806–1817

Igarashi M, O-Uchi T, Alford BR (1981) Volumetric and dimensional measurements of vestibular strucutres in the squirrel monkey. Acta Otolaryngol 91:437–444

Igarashi M, O-Uchi T, Isago H, Wright WK (1983) Utricular and saccular volumetry in human temporal bones. Acta Otolaryngol 95:75–80

Ito M (1984) The cerebellum and neural control. Raven Press, New York

Ito M, Nisimaru N, Yamamoto M (1973) The neural pathways mediating reflex contraction of extraocular muscles during semicircular canal stimulation in rabbits. Brain Res 55:183–188

Ito M, Nisimaru N, Yamamoto M (1976) Pathways for vestibulo-ocular reflex excitation arising from semicircular canals of rabbits. Exp Brain Res 24:273–283

Kasahara M, Uchino Y (1974) Bilateral semicircular canal inputs to neurons in cat vestibular nuclei. Exp Brain Res 20:285–296

Landolt JP, Correia MJ (1980) Neurodynamic response analysis of anterior semicircular canal afferents in the pigeon. J Neurophysiol 43:1746–1762

Lorente de Nó R (1933) Vestibulo-ocular reflex arc. Arch Neurol Psychiat 30:245–291

Lowenstein O, Sand A (1940) The mechanism of the semi-circular canals: a study of single fiber prepartaions to angular acceleration and to rotation at constant speed. Proc R Soc Lond B Biol Sci 129:256–275

Mach E (1875) Grundlinien der Lehre von den Bewegungsempfindugen. Engelmann, Leipzig

Makhijani VB, Yang HQ, Srinivasan K, Grant JW (1996) Mechanical interactions between the cupula, endolymph and

otoliths in the horizontal semicircular canal in the vestibular labyrinth. Assoc Res Otolaryngol, St. Petersburg Beach, Fla

Markham CH, Curthoys IS (1972) Labyrinthine convergence on vestibular nuclear neurons using natural and electrical stimulations. In: Brodal A, Popeiano O (eds) Basic aspects of central vestibular mechanisms. Elsevier, New York, pp 128–187

McCrea RA, Yoshida K, Berthoz A, Baker R (1980) Eye movement related activity and morphology of second order vestibular neurons terminating in the cat abducens nucleus. Exp Brain Res 40:468–473

McCrea RA, Strassman A, May E, Highstein SM (1987a) Anatomical and physiological characteristics of vestibular neurons mediating the horizontal vestibulo-ocular reflex of the squirrel monkey. J Comp Neurol 264:547–570

McCrea RA, Strassman A, Highstein SM (1987b) Anatomical and physiological characteristics of vestibular neurons mediating the vertical vestibulo-ocular reflex of the squirrel monkey. J Comp Neurol 264:571–594

Money KE, Sokoloff M, Weaver RS (1966) Specific gravity and viscosity of endolymph and perilymph. In: Second symposium on the role of the vestibular organs in space exploration vol 115. NASA SP-115 Pensacola pp 91–97

Money KE, Bonen L, Beatty JD, Kuehn LA, Sokoloff LA, Weaver RS (1971) Physical properties of fluids and structures of vestibular apparatus of the pigeon. J Am Physiol 110:140–147

Mow VC, Mak A, Lai WM, Rosenberg LC, Tan L-H (1984) Viscoelastic properties of proteoglycan subunits and aggregates in varying solution concentrations. J Biomech 17:325–338

Muller M, Verhagen JHG (1988a) A mathematical approach enabling the calculation of the total endolymph flow in the semicircular ducts. J Theor Biol 134:503–529

Muller M, Verhagen JHG (1988b) A new quantitative model of total endolymph flow in the system of semicircular ducts. J Theor Biol 134:473–501

O'Leary DP, III C Wall (1979) Analysis of nonlinear afferent response properties from the guitarfish semicircular canal. Adv Oto-Rhino-Laryngol 1977:66–73

Oman CM, Marcus EN, Curthoys IS (1987) The influence of semicircular canal morphology on endolymph flow dynamics. Acta Otolaryngol 103:1–13

Pellionisz A, Graf W (1987) Tensor network model of the three-neuron vestibulo-ocular reflex arc in cat. J Theor Neurobiol 5:127–151

Pellionisz A, Llinäs R (1980) Tensorial approach to the geometry of brain function: cerebellar coordination via a metric tensor. Neuroscience 5:1125–1136

Peterson BW, Baker JF, Perlmutter SI, Iwamoto Y (1992) Neuronal substrates of spatial transformations in vestibuloocular and vestibulocollic reflexes. In: Cohen B, Tomko DL, Guedry F (eds) Sensing and controlling motion: Vestibular and sensorimotor function, vol 656. Ann NY Acad Sci, pp 485–499

Rabbitt RD, Boyle R, Highstein SM (1994) Sensory transduction of head velocity and acceleration in the toadfish horizontal semicircular canal. J Neurophysiol 72:1041–1048

Rabbitt RD, Boyle R, Highstein SM (1998) Responses of patent and plugged semicircular canals to linear and angular acceleration. Soc Neurosci Abstr 24:1653

Reisine H, Simpson JI, Henn V (1988) A geometric analysis of semicircular canals and induced activity in their peripheral afferents in the rhesus monkey. Ann NY Acad Sci 445:163–172

Robinson DA (1982) The use of matrices in analyzing the three-dimensonal behavior of the vestibulo-ocular reflex. Biol Cybern 46:53–66

Sans A, Raymond J, Marty R (1972) Projections des crêtes ampullaires et de l'utricle dans les noyaux vestibularies primarires: étude microphysiologique et corrélations anatomo-functionelles. Brain Res 44:337–355

Schneider LW, Anderson DJ (1976) Transfer characteristics of first and second order lateral canal vestibular neurons in gerbil. Brain Res 112:61–76

Segal BN, Outerbridge JS (1982) Vestibular (semicircular canal) primary neurons in the bullfrog: Nonlinearity of individual and population response to rotatio. J Neurophysiol 47:545–562

Silver RB, Reeves AP, Steinacker A, Highstein SM (1998) Examination of the cupula and stereocilia of the horizontal semicircular canal in the toadfish, *Opsanus tau*. J Comp Neurol 402(1):48–61

Simpson JI, Leonard CS, Soodak RE (1988) The accessory optic system: Analyser of self-motion. In: Cohen B, Henn V (eds) Representation of three-dimensional space in the vestibular, oculomotor, and visual systems, vol 545. Ann NY Acad Sci, pp 545:170–179

Steer RW Jr, Li YT, Young LR (1967) Physical properties of the labyrinthine fluids and quantification of the phenomenon of caloric stimulation. In: Third symposium on the role of the vestibular organs in space exploration, vol 152, NASA SP-152, Pensacola. pp 409–420

Steinhausen W (1933) Über die Beobachtungen der Cupula in den Bogengangsampullen des Labyrinthes des lebenden Hechts. Pflügers Arch 232:500–512

Suzuki JI, Cohen B (1964) Head, eye, body and limb movements from semicircular canal nerves. Exp Neurol 10:393–405

Suzuki JI, Goto K, Tokumasu K, Cohen B (1969) Implantation of electrodes near individual nerve branches in mammals. Ann Otol (St Louis) 68:350–362

Szentágothai J (1950) The elementary vestibulo-ocular reflex arc. J Neurophysiol 13:395–407

Uchino Y, Suzuki S, Miyazawa T, Watanabe S (1979) Horizontal semicircular canal inputs to cat extraocular motoneurons. Brain Res 177:231–240

Uchino Y, Suzuki S, Watanabe S (1980) Vertical semicircular canal inputs to cat extraocular motoneuron. Exp Brain Res 41:45–53

Vidal PP, Graf W, Berthoz A (1986) The orientaion of the cervical vertebral column in unrestrained awake animals. i. Resting position. Exp Brain Res 61:549–559

Waespe W, Henn V (1977) Neuronal activity in the vestibular nuclei of the alert monkey during vestibular and optokinetic stimulation. Exp Brain Res 27:523–538

Wersäll J, Bagger-Sjöbäck D (1974) Morphology of the vestibular sense organ. In: Kornhuber HH (ed) Handbook of Sensory Physiology: vestibular system. Springer, Berlin Heidelberg New York, pp 123–170

Wilson VJ, Felpel LP (1972) Specificity of semicircular canal input to neurons in the pigeon vestibular nuclei. J Neurophysiol 35:253–264